Rare Metal Materials and Engineering
Volume 53, Issue 11, November 2024
Available online at www.rmme.ac.cn

Science Press

Cite this article as: Luo Jiajun, Quan Ciwang, Zhang Jianjun, et al. Preparation and Characterization of Core-Shell $MoSi_2$@Nb Materials Sintered by SPS[J]. Rare Metal Materials and Engineering, 2024, 53(11): 3053-3063. DOI: 10.12442/j.issn.1002-185X.20240105.

ARTICLE

Preparation and Characterization of Core-Shell $MoSi_2$@Nb Materials Sintered by SPS

Luo Jiajun[1], Quan Ciwang[1], Zhang Jianjun[1,2], Chen Shuixiang[1], Zhang Xitong[1], Han Mengyao[1], Liang Bingliang[1], Chen Weihua[1]

[1] School of Materials Science and Engineering, Nanchang Hangkong University, Nanchang 330063, China; [2] Jiangxi Provincial Engineering Research Center for Surface Technology of Aeronautical Materials, Nanchang Hangkong University, Nanchang 330063, China

Abstract: Core-shell $MoSi_2$@Nb powder was prepared by electrostatic layer self-assembly method. The surfactants SDS ($CHSO_4Na$) and CTAB ($C_{19}H_{42}BrN$) were used to modify the surface of the two particles to make them charged, and the Zeta potential of the suspension was tested by the Zeta potentiometer. Scanning electron microscope, transmission electron microscope and energy dispersive spectrometer were used to characterize the phase, morphology, microstructure and element distribution of synthetic materials. The results show that when the SDS concentration is 2 mmol/L, the CTAB concentration is 3mmol/L and the pH value of Nb suspension is 5, the coating effect is better after secondary cladding. $NbSi_2$ phase is found at the interface between Nb and $MoSi_2$ after calcination at 200 °C for 2 h in Ar atmosphere, indicating that Nb is highly active and reacts with Si. Core-shell structure is still retained in $MoSi_2$@Nb material after spark plasma sintering at 1450 °C for 2 h under uniaxial pressure of 40 MPa. However, it is found that Nb reacts strongly with $MoSi_2$, and most of the Nb phase is reacted. This issue needs to be addressed in subsequent studies. The fracture toughness (K_{IC}) of $MoSi_2$@Nb material is significantly improved to 5.75 MPa·$m^{0.5}$ compared with that of $MoSi_2$ material (3.32 MPa·$m^{0.5}$).

Key words: core-shell structure; electrostatic layer self-assembly; spark plasma sintering; fracture toughness

Molybdenum disilicide, as a promising next generation high-temperature structural material, has high melting point (2030 °C), lower density (6.24 g/cm^3) and excellent oxidation resistance at high temperatures[1–3]. $MoSi_2$ has a great prospect of application in the aerospace field for its high work temperature which is far higher than the highest service temperature of nickel-based superalloy (<1100 °C)[4–5]. However, its high tough-brittle transition temperature (BDTT=1000 °C) results in greater brittleness below 1000 °C. Moreover, the creep resistance is poor when work temperature is higher than 1200 °C[6]. These deficiencies need to be addressed for broadening the applications of $MoSi_2$ materials.

Nb has the characteristics of high melting point, good high-temperature strength and low-temperature plasticity[7], which has been widely used in superalloys as a reinforcing element, and can be alloyed and compounded with $MoSi_2$. However, the toughness of $MoSi_2$ is limited when using Nb as the alloying enhancement element alone. When different forms of Nb and $MoSi_2$ are used for composite toughening, the crack will be deflected by the particle-reinforced phase, and the fracture toughness of the matrix can be increased by 20%–30%. The fibrous ductile phase will passivate the crack tip and bridge the crack, and the toughness of the matrix will be increased by 100%–300%. The laminate structure consisting of plastic phase and $MoSi_2$ can increase the fracture toughness of the matrix by 400%–500%, so as to achieve better room temperature toughness. Studies have shown that adding the second phase particles, such as ZrO_2[8], SiC[9], $NbSi_2$[10] and Nb[11], can improve the microstructure, refine the grain and prevent the crack growth, thus improving the mechanical properties of $MoSi_2$. Dasgupta et al[12] prepared $MoSi_2$-based composite ceramics doped with a certain amount of Nb and Al

Received date: February 29, 2024
Foundation item: National Natural Science Foundation of China (51861026); The Graduate Innovation Special Fund of Nanchang Hangkong University (YC2022-011)
Corresponding author: Zhang Jianjun, Ph. D., Associate Professor, School of Materials Science and Engineering, Nanchang Hangkong University, Nanchang 330063, P. R. China, E-mail: zhangjiajun@nchu.edu.cn

elements by arc melting and hot pressing sintering. They found that the mechanical properties of $(Mo_{0.99}Nb_{0.01})(Si_{0.96}Al_{0.04})_2$ composite ceramics were significantly improved compared with that of the un-doped $MoSi_2$. At room temperature, the hardness and rigidity of $(Mo_{0.99}Nb_{0.01})(Si_{0.96}Al_{0.04})_2$ composite ceramics were lower. Accordingly, the fracture toughness increased from 3.33±3 MPa·$m^{1/2}$ to 4.05± 0.3 MPa·$m^{1/2}$, and the fracture mode is mainly transgranular fracture. Zenk et al[13] prepared $MoSi_2$-based composite ceramics doped with appropriate amount of Nb, Al and Ta elements by arc melting. From a microscopic point of view, the influence of elements on the sliding system of $MoSi_2$ was studied at low temperature. The results show that the microhardness of the composite ceramics, which was doped with Nb, Al and Ta elements, is smaller than that of the pure $MoSi_2$ ceramic. The dislocation lines around the micro-indentation were analyzed by transmission electron microscope (TEM), and results showed that the {110} <111> slip system was activated at room temperature due to the addition of Nb, Al and Ta elements, while the slip system could not be activated in pure $MoSi_2$ until above 300 °C. This is sufficient to infer that the doping of Nb can make $MoSi_2$ have more slip planes at room temperature, thus achieving better toughness. However, due to the limited alloying ability of $MoSi_2$, the improvement in toughness of fracture is restricted. Nb has a high melting point (2468 °C) and good toughness, which was used as a toughness enhancement phase to $MoSi_2$[14]. It is also a means to improve the toughness of $Mosi_2$ at room temperature.

Nowadays, there are a large number of researches on core-shell structural materials, and it is obtained that the construction of core-shell structure is beneficial to combine the properties of various materials to achieve the additive effect. At the same time, because shell material is evenly distributed on the surface of nuclear material particles, it can protect nuclear materials. So it has a great application prospect in biomedicine, coating materials and other fields[15–16]. Zhu et al[17] synthesized a new multilayer fluorescent microsphere PS@CdTe using the electrostatic layer self-assembly technique. The surface of the PS sphere is positively charged after adding cationic surfactant CTAB, which can attract CdTe quantum dots (QDs) with a negative charge. When the pH value of the buffer solution is 7.8, the negative charge on the surface of CdTe QDs reaches the maximum, which is favorable for the synthesis of electrostatic self-assembled microspheres. The fluorescence properties of PS@CdTe microspheres gradually increased with the increase in the number of coating layers, and the optimal number of coating layers was 3.

In this study, the core-shell $MoSi_2$@Nb powders were prepared by electrostatic layer-by-layer self-assembly method. Then, the prepared core-shell $MoSi_2$@Nb powder was sintered by spark plasma sintering (SPS). The phases, microstructures and mechanical properties of $MoSi_2$@Nb and $MoSi_2$ material sintered by SPS with the same process were also studied.

1 Experiment

1.1 Materials

The materials used in the preparation included commercially available $MoSi_2$ powder (powder size: 3 μm; purity: >99.5%; Beijing Xingrongyuan Technology Co., Ltd), sodium dodecyl sulfate SDS ($CHSO_4Na$; purity: 99%; Tianjin Beichen Founder Reagent Factory), commercially available spherical Nb powder (powder size: 50 nm; purity: 99.9%; Shanghai Pantian Nanotech Co., Ltd), cetyltrimethyl ammonium bromide CTAB ($C_{19}H_{42}BrN$; purity: 99%, Shanghai Macklin Biochemical Co., Ltd), dilute hydrochloric acid and sodium hydroxide (3.5wt%, prepared in the laboratory).

1.2 Preparation of $MoSi_2$@Nb core-shell powders and material

Raw $MoSi_2$ powder was modified by high-energy ball milling with an omnidirectional planetary ball mill. The carbide balls with 5 and 7 mm in diameter were used as grinding balls, and mass ratio was 4: 1. The $MoSi_2$ and grinding balls with mass ratio of 15:1 were put into 500 mL carbide ball grinding tanks that were fed with an appropriate amount of protective Ar gas. Then, ball grinding tanks were fixed on the ball mill and $MoSi_2$ powders were ground at 150 r/min for 12 h. The $MoSi_2$ powder finished by ball milling was ground and sieved through 200# sieve.

First, 1.5 g Nb powder was weighed and dispersed in 90 mL distilled water by a constant speed mechanical stirrer at 600 r/min with an ultrasonic cleaner for 30 min. Then, 0.1006 g CTAB was added and stirred for 15 min to prepare Nb suspension for later use. The pH value of the Nb suspension was adjusted to 5 by dilute hydrochloric acid. 8.5 g ball-milled $MoSi_2$ powder was mixed with 255 mL distilled water and ultrasonically stirred at 600 r/min for 30 min with a constant speed mechanical stirrer and ultrasonic cleaner. 0.1522 g SDS was added to the powder and then stirred with ultrasonic stirring for 15 min. Then, the prepared Nb suspension was added into the $MoSi_2$ suspension followed by ultrasonic stirring for 30 min. The prepared suspension was extracted and filtered to get once-coated $MoSi_2$@Nb powder, which was dissolved into 255 mL distilled water again. The coating process was repeated, and then the twice-coated $MoSi_2$@Nb powder was prepared after extracting, filtering, vacuum drying and calcining, and extracting, filtering and vacuum drying again. Fig.1 shows a concise flow chart of the preparation process of $MoSi_2$@Nb powders. 4 g $MoSi_2$@Nb and ball-milled $MoSi_2$ powders were taken and sintered into $MoSi_2$@Nb and $MoSi_2$ materials, respectively by SPS (SPS-3T-3-MiNi (H)) with a ramp-up rate of 100 °C/min, and then they were ramped down to 1450 °C and held for 10 min under a uniaxial pressure of 40 MPa which was maintained during the ramp-up and holding processes.

1.3 Characterization

Zeta potentials of $MoSi_2$ suspension, Nb suspension and mixed suspension with surfactants were measured by Zeta potentiometer (NanoBrook 90Plus PALS). Particle size

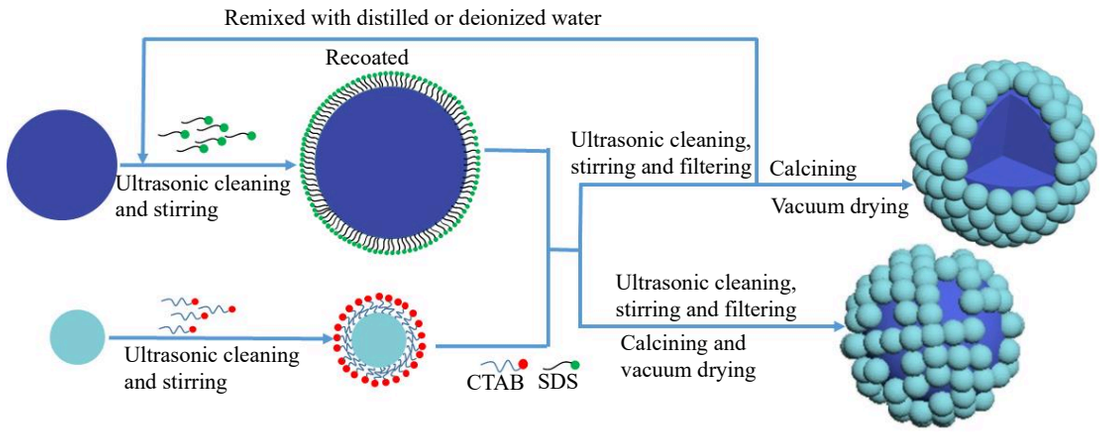

Fig.1 Schematic diagram of electrostatic layer-by-layer self-assembly preparation of $MoSi_2$@Nb

distribution of raw Nb and ball-milled $MoSi_2$ powders was measured by laser particle size analyzer (NanoBrook 90Plus PALS). X-ray diffractometer (XRD, D8, ADVANCE) was used to detect the phase of ball-milled $MoSi_2$ powder, $MoSi_2$@Nb powder and sintered samples. Scanning electron microscope (SEM, FEI Nova Nano SEM450) was used to observe the morphology of $MoSi_2$@Nb powders. Energy dispersive spectrometer (EDS, INCA 250 X-Max 50) was used to detect the distribution of elements and to characterize the core-shell structure. To further observe the microscopic details at the interface between Nb and $MoSi_2$ particles, field emission TEM (Talos F200X) was used to characterize twice-coated $MoSi_2$@Nb powder. The Vickers hardness of $MoSi_2$@Nb and $MoSi_2$ materials was measured with a Vickers hardness tester under a load of 1 kg for 15 s. The density of $MoSi_2$@Nb and $MoSi_2$ materials was measured by the Archimedes drainage method. The fracture toughness (K_{IC}) of the samples was measured by hardness test under a load of 10 kg for 15 s with crack length and calculated through the formula reported by Niihara et al[18–19]:

$$\left(\frac{K_{IC}\Phi}{H\sqrt{d}}\right)\left(\frac{H}{E\Phi}\right)^{0.4} = 0.035\left(\frac{l}{d}\right)^{-1/2} \quad (1)$$

where d is the diagonal half length of the indentation (mm); H is the Vickers hardness value (GPa); Φ is the constraint factor ($\Phi \approx 3$); E is the elastic modulus of the composite material (GPa); l is the crack length (mm). E is obtained from Eq.(2):

$$E = V_{MoSi_2}E_{MoSi_2} + V_{Nb}E_{Nb} \quad (2)$$

where E_{MoSi_2} and E_{Nb} are the elastic moduli of $MoSi_2$ and Nb, respectively; V_{MoSi_2} and V_{Nb} are the volume fractions of $MoSi_2$ and Nb, respectively[20].

2 Results and Discussion

2.1 Morphology and Zeta potential of materials

The morphologies of raw $MoSi_2$ and ball-milled $MoSi_2$ powders are shown in Fig.2a–2c and Fig.2d, respectively. Nb powder was not pretreated, and its morphology is shown in Fig.2e–2f. It can be seen that $MoSi_2$ particles after ball milling have smooth surface, regular shape and smaller and more uniform particle size. The size of Nb particles is relatively uniform and its shape is spherical. As we all know, the surface of solid particles is easy to absorb other substances. Besides, the amount of charge of solid particle is closely related to its size and shape. When powder particles are in the liquid medium, the surface of the particle and liquid interface will produce ionization, ion adsorption and lattice substitution, so the particle will be electrically charged[21–22]. As shown in Fig. 3a, the average particle size of the raw Nb powder is 193.89 nm. There are two peaks of 324.07 and 1409.08 nm in the particle size distribution curve of ball-milled $MoSi_2$ powder. Therefore, it indicates that $MoSi_2$ powder is refined by high energy ball milling. Moreover, the surface energy of equal mass powder will increase as the particles size decreases, which is more conducive to the adsorption of surfactant.

Fig. 3b shows the Zeta potential values of $MoSi_2$ and Nb suspensions with surfactants. The potential of $MoSi_2$ particles becomes more negative after mixing with SDS, which is because the SDS molecule is negatively charged, and the Zeta potential value reaches the maximum of –46.28 mV when the SDS concentration is 2 mmol/L. Compared with the suspension of $MoSi_2$ without SDS, there is a significant increase in the Zeta potential value. Similarly, Nb particles become positively charged after mixing with CTAB possessing positive charge. The potential of Nb+CTAB suspension is significantly higher than that of Nb suspension. It is found that when the concentration of CTAB is 3 mmol/L, the maximum value of Zeta potential is 18.09 mV, and its absolute value is less than 30. For electrostatic adsorption, the absolute value of the opposite charge between particles plays a decisive role. Moreover, the absolute value of Zeta potential also reflects the dispersion degree of suspension. The larger the absolute value of potential, the better the dispersion effect, until reaching an extreme value. pH value has a significant effect on the adsorption of some surfactants on the particle surface, which directly affects the Zeta potential value[23–24]. Aimed on improving the surface charge of Nb particles, the effect of pH on the Zeta potential of Nb suspension is

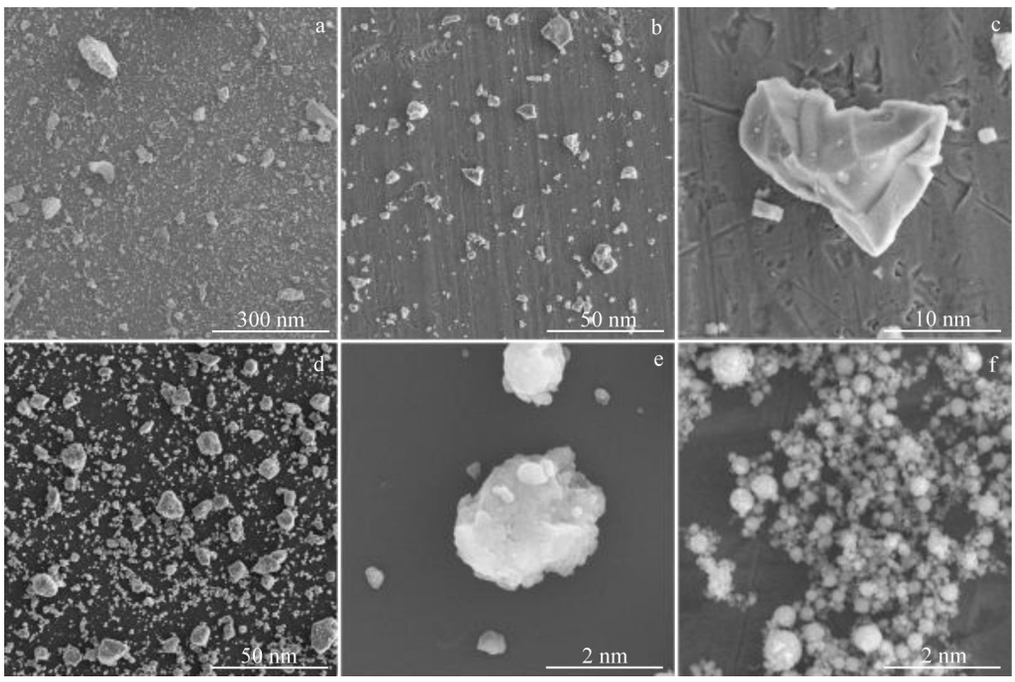

Fig.2 Microstructures of purchased $MoSi_2$ powder (a–c), ball-milled $MoSi_2$ powder (d), and purchased Nb powder (e–f)

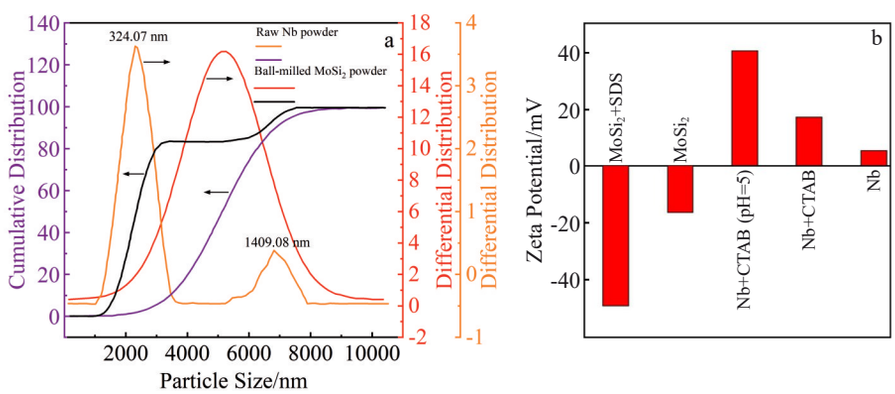

Fig.3 Particle size distribution of raw Nb and ball-milled $MoSi_2$ powders (a); Zeta potential values of $MoSi_2$ and Nb suspensions mixed without and with surfactant (b)

considered. A series of Nb suspensions with different pH values were modulated by dilute hydrochloric acid and sodium hydroxide, and the results are shown in Fig. 3b. It can be found that the Zeta potential value of Nb suspensions with CTAB concentration of 3 mmol/L can reach 40.06 mV when the pH value is 5. Then, the mass fraction of Nb is 15wt% for primary coating, and the suspension with the same mass of Nb is prepared for secondary coating.

2.2 Core-shell structure of $MoSi_2$@Nb powders

Fig. 4 shows the morphologies of once-coated and twice-coated $MoSi_2$@Nb powders. Fig.4a–4c show the surface morphologies of once-coated powder. It can be observed that small spherical particles are attached to the surface of $MoSi_2$ particle, which correspond to the morphology of the raw Nb powder, but the amount of Nb particles is not much. The morphologies of the twice-coated powder are shown in Fig. 4d–4f. It can be seen that the surface of $MoSi_2$ particle is almost wrapped by spherical Nb particles. Fig. 4g – 4i show EDS element mappings, which further support the above analysis. The Nb elements are mainly distributed around Mo and Si elements. Because the $MoSi_2$ particles are surrounded by Nb particles, and Nb element also exists in the middle of the $MoSi_2$ surface, the coating effect of twice-coated $MoSi_2$@Nb is better, and the microstructure of the interface between Nb and $MoSi_2$ particles should be further observed to explain the coating effect.

Fig.5 shows TEM images and EDS analysis results of twice-coated powder. It can be seen that area 1# is mainly $MoSi_2$ with a small amount of Nb. This indicates that Nb is adsorbed on the particle surface, which agrees with the scanning results. From results of area 2#, it can be seen that spherical Nb particles are adsorbed on the edge of $MoSi_2$ particles. Fig. 5e–5g are EDS element mappings corresponding to Fig. 5b, showing the distribution of Mo, Si and Nb, respectively. Mo

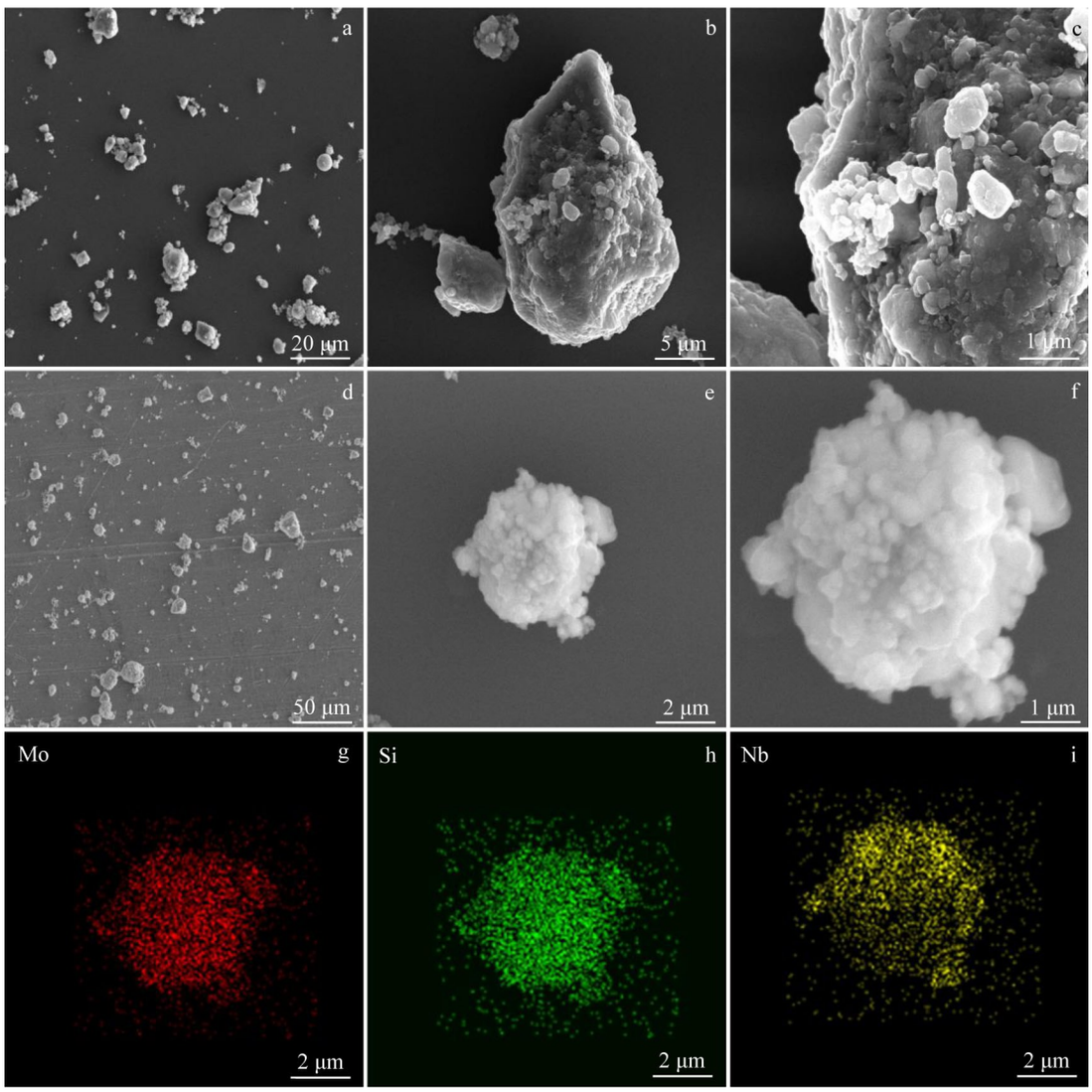

Fig.4 Microstructures of once-coated (a–c) and twice-coated (d–f) $MoSi_2$@Nb powders; EDS element mappings of Mo (g), Si (h) and Nb (i) corresponding to Fig.4e

and Si elements are uniformly distributed around the $MoSi_2$ particles, while Nb element is uniformly and relatively completely distributed outside the Mo and Si elements, forming a core-shell structure and achieving a better coating effect.

As shown in Fig. 6, compared to the XRD pattern of ball-milled $MoSi_2$ powder, not only Nb phase but also $NbSi_2$ phase is detected for $MoSi_2$@Nb powder, which may be interaction products between $MoSi_2$ and Nb particles during the calcination at 200 °C for 2 h. More details need to be found to prove it. Fig. 7 shows the high resolution TEM (HRTEM) image of twice-coated $MoSi_2$@Nb powder and corresponding SEAD patterns. In Fig. 7a, it can be found that in addition to Nb phase, $NbSi_2$ phase is also found compared with the microstructure of $MoSi_2$ powder after ball milling. Due to the strong chemical compatibility between Nb and $MoSi_2$, atoms still migrate at low temperatures, resulting in this hybrid phase. Fig. 7a shows the HRTEM image of coated powder particles. Three different regions can be clearly divided at the interface between $MoSi_2$ particles and spherical Nb particles. Fig. 7b and 7c show SAED patterns corresponding to area 1# and area 2#, respectively. Area 1# can be determined as $MoSi_2$ by calibration analysis and the corresponding strip axis is [110]. Area 2# is determined as Nb and the corresponding strip axis is $[\bar{1}11]$. Area 3# is another substance formed by $MoSi_2$ and Nb. Fig. 7d is inverse fast Fourier transform (IFFT) pattern of area 3# obtained by digital micrograph software. It can be determined to be $NbSi_2$ by XRD analysis and calibration and the corresponding strip axis is $[7\,\bar{1}3]$.

2.3 Phase and mechanical properties of $MoSi_2$@Nb and $MoSi_2$ materials

Phase analysis of the once-coated and twice-coated $MoSi_2$@Nb as well as the $MoSi_2$ materials are shown in Fig. 8. We can find that the characteristic peaks of Nb phase are very low (38.4744° and 55.540°), indicating that Nb has a sharp reaction with the matrix $MoSi_2$. By comparing the phases of the primary coating and the secondary coating, it can be found

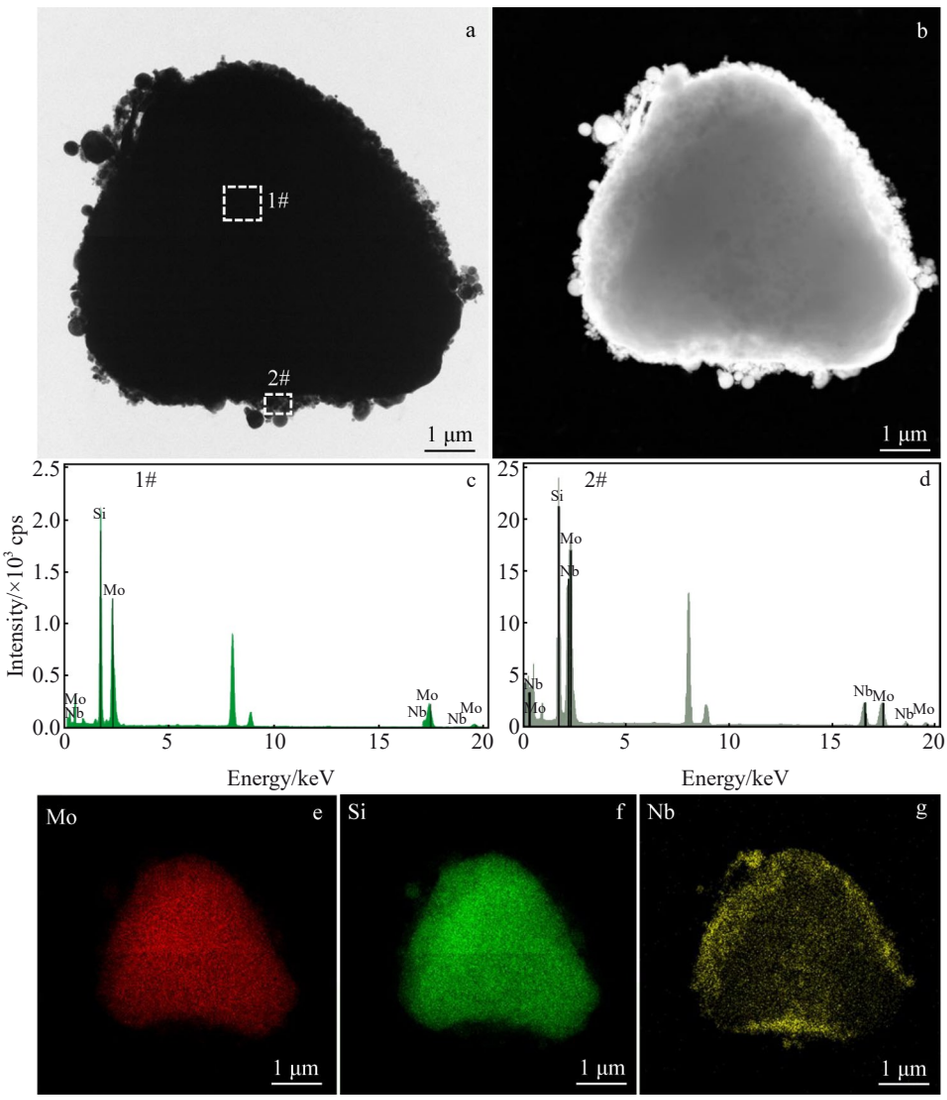

Fig.5 TEM images of twice-coated $MoSi_2$@Nb powder with core-shell microstructures (a–b); EDS spot scanning results of area 1# (c) and area 2# (d) marked in Fig.5a; EDS element mappings of Mo (e), Si (f), and Nb (g)

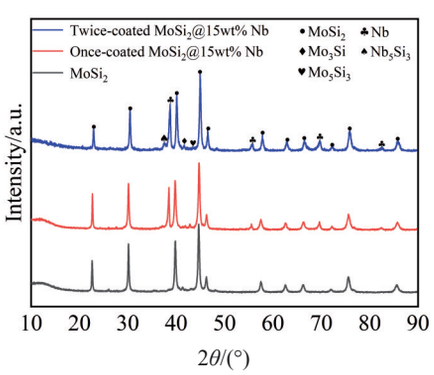

Fig.6 XRD patterns of ball-milled $MoSi_2$ and $MoSi_2$@Nb powders

that the primary coating material produces more products during the sintering process, so it can be inferred that the effect of the primary coating is too low to hinder the reaction between $MoSi_2$ and Nb. The main phases of $MoSi_2$@Nb materials are $MoSi_2$, Mo_5Si_3, Nb_5Si_3 and $NbSi_2$. Because the powders absorb a small amount of air and cannot be discharged, a small amount of Nb_2O_5 phase is produced after SPS. In $MoSi_2$ material, Mo_5Si_3 and SiO_2 phases are produced, which stem from the reaction between $MoSi_2$ and O_2[25]. Therefore, there are also SiO_2 phases in $MoSi_2$@Nb materials.

The microstructure of $MoSi_2$@Nb and $MoSi_2$ materials were further characterized by SEM, and the results are shown in Fig. 9. Fig 9a–9c show the microstructures of twice-coated $MoSi_2$@Nb material and Fig. 9g shows the microstructure of the primary coating. It can be seen that the void of the secondary coatings is significantly lower than that of the primary coating, suggesting that the compactness of the secondary coatings is higher, which is conducive to improvement in the fracture toughness of the material. Fig.9d–9f show the EDS element mappings corresponding to Fig. 9b. It can be seen that Nb element is mainly distributed around Si element, while Mo element is distributed in a wide range. At 1450 °C, Mo, Nb and Si elements are active, and the diffusion ability of Si is stronger than that of Mo. As can be seen from

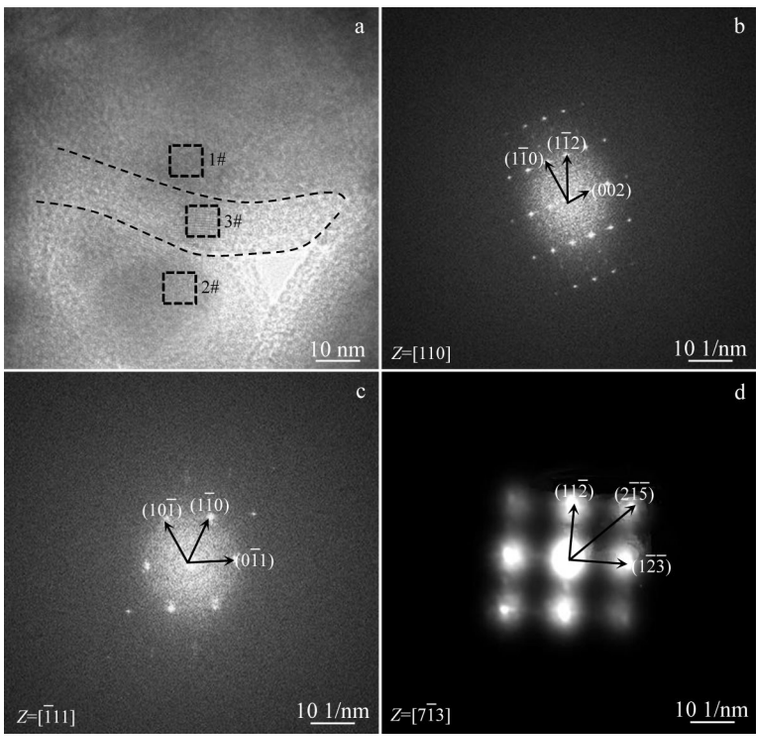

Fig.7 HRTEM image (a), SEAD patterns (b–c), and IFFT pattern (d) of twice-coated $MoSi_2$@Nb powder with core-shell microstructure: (b) area 1#, (c) area 2#, and (d) area 3#

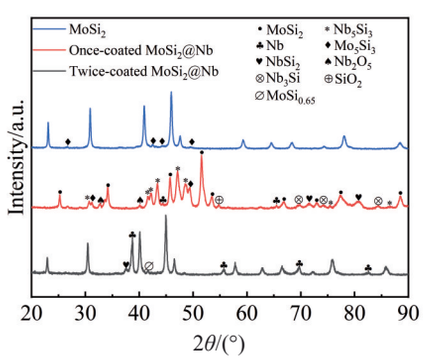

Fig.8 XRD patterns of $MoSi_2$@Nb block materials

the EDS results, Si element is distributed in the black structure, and there is strong mutual diffusion between Nb and Mo. As a result, Mo and Nb react sharply, and the following reactions may occur at 1450 °C[26–27] :

$$35MoSi_2+35Nb=20NbSi_2+7Mo_5Si_3+3Nb_5Si_3 \quad (3)$$

$$xMo_5Si_3+(1-x)Nb_5Si_3=(Mo_x, Nb_{1-x})_5Si_3 \quad (4)$$

Table 1 shows the point scanning results of spots marked in Fig. 9, and three types of structures can be clearly seen from Fig. 9a. Combined with the above analysis, it can be determined that grayish black structure is $MoSi_2$ and it is coated with grayish white structure. The composition of the grayish structure is mainly $(Mo, Nb)_5Si_3$, with a small number of Nb. The black structure is mainly randomly distributed in the grayish white structure. There are a small number of holes in the black structure, which may be caused by the large volume shrinkage caused by Nb reacting with $MoSi_2$. Excluding the pores, the composition of black structures is mainly $NbSi_2$ and Nb_3Si with a small amount of Si. Although Nb reacts sharply with $MoSi_2$, Nb and Nb compounds with Mo and Si are distributed around $MoSi_2$ grains. Hence, $MoSi_2$@Nb materials retain core-shell structure after SPS at 1450 °C for 10 min under a uniaxial pressure of 40 MPa. It can be determined from Fig. 9c that the white structure is Mo_5Si_3 and the black structure is holes and Si.

It is known that the elastic moduli of $MoSi_2$, Nb, Mo_5Si_3 and $NbSi_2$ are 420, 105, 263 and 362 GPa, respectively. The elastic modulus values of Nb, Nb silicides and Mo silicides are lower than that of $MoSi_2$, indicating that the reaction products of Nb and $MoSi_2$ can affect the fracture toughness[10]. $MoSi_2$@Nb material has high toughness because the effect of Nb, Nb_5Si_3, Mo_5Si_3 and $NbSi_2$ multiphase toughening $MoSi_2$, and the good toughness of Nb phase can make the crack tip form a plastic deformation zone or a ductile crack bridging. However, the fracture of $(Mo, Nb)_5Si_3$, which is slightly tougher than that of $MoSi_2$, can produce a synergistic effect and play a diffusion strengthening role at the $MoSi_2$ grain boundary. The fracture resistance of a material needs to be measured by the fracture toughness (K_{IC}), so the microscopic indentations of $MoSi_2$ and $MoSi_2$@Nb materials are shown in Fig. 10a–10b, respectively, which are the source of the crack. Fig. 11a shows the Vickers hardness, relative density and fracture toughness of $MoSi_2$ and $MoSi_2$@Nb materials. Fig.11b – 11c show the grain size distribution of $MoSi_2$ and twice-coated $MoSi_2$@Nb with core-shell structure, respectively. It can be found that the average grain size of $MoSi_2$ is reduced

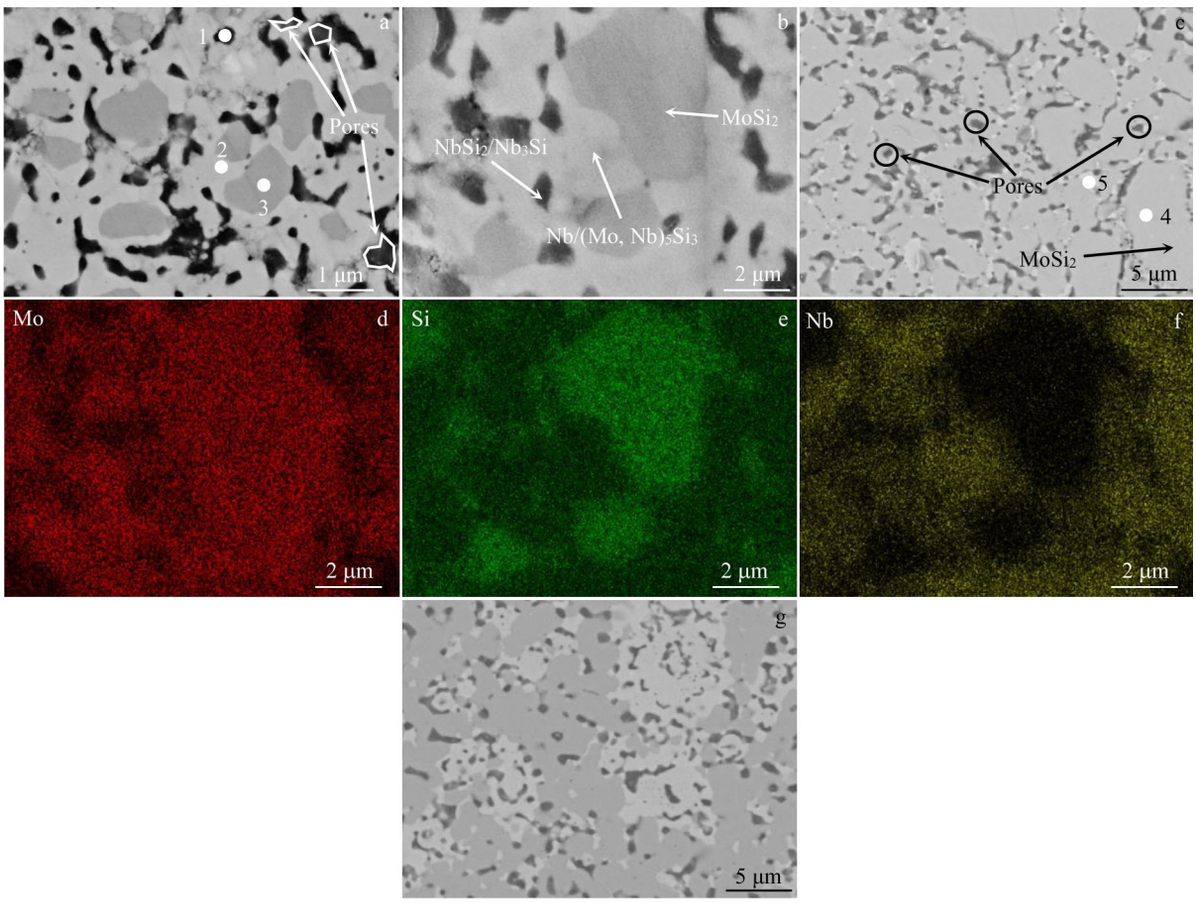

Fig.9 SEM images of microstructure of twice-coated $MoSi_2$@Nb (a–c); EDS element mappings corresponding to Fig.9b (d–f); SEM image of microstructure of once-coated $MoSi_2$@Nb (g)

Table 1 EDS point scanning result of spots marked in Fig. 9a and 9c (at%)

Spot	Mo	Si	Nb
1	30.57	69.43	-
2	20.88	44.49	34.63
3	5.31	82.62	12.07
4	34.47	65.53	-
5	60.66	39.44	-

from 3.84 μm in $MoSi_2$ material to 2.61 μm in $MoSi_2$@Nb material, the Vickers hardness increases from 12.09 GPa to 12.52 GPa, and the fracture toughness increases from 3.32 MPa·$m^{1/2}$ to 5.75 MPa·$m^{1/2}$. For the once-coated $MoSi_2$@Nb with core-shell structure, the fracture toughness is 4.77 MPa·$m^{1/2}$ and the Vickers hardness is 12.19 GPa, which are not much improved. Compared to the effect of single coating, the problem of low single coating rate can be solved by secondary coating, and increasing the coating rate can better protect $MoSi_2$, avoid the oxidation of $MoSi_2$ into MoO_3, reduce the pores left by the volatilization of MoO_3 at high temperatures and improve the mechanical properties of the material. According to Table 2, it can be seen that the fracture toughness of secondary coating is greatly improved compared

Fig.10 Vickers indentation patterns of $MoSi_2$ material (a), twice-coated $MoSi_2$@Nb material (b), and once-coated $MoSi_2$@Nb material (c)

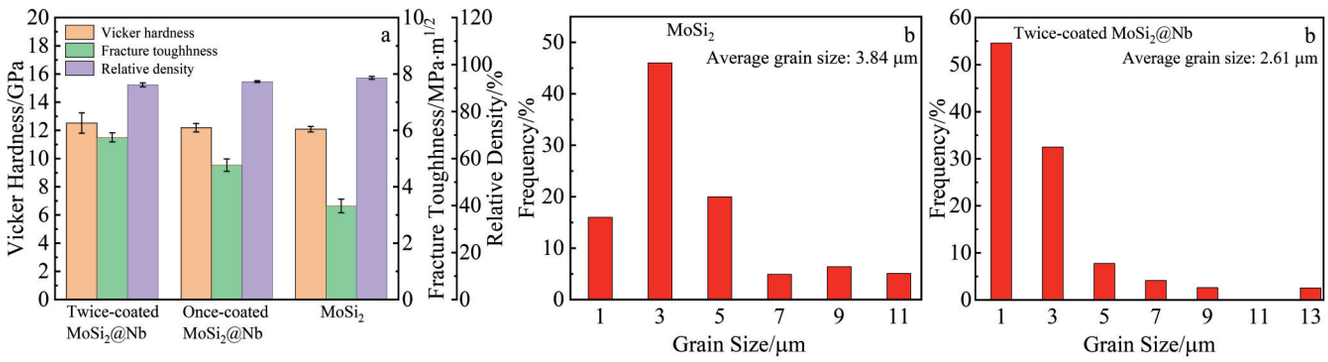

Fig.11 Mechanical properties (a) and grain size distributions (b–c) of $MoSi_2$ and $MoSi_2$@Nb materials

with that of primary coating and directly mixed $MoSi_2$ materials[28]. In theory, grain refinement will improve the hardness greatly, but $MoSi_2$@Nb material has a small increase in hardness. This may be due to lower density compared with that of $MoSi_2$ material. The presence of more pores will lead to low adhesion between grains, resulting in lower hardness. while fine grains increase the number of grain boundaries in the same volume, which is not easy to produce stress concentration, making the material have better toughness.

It will be beneficial to improve the K_{IC} value of the material while effectively preventing the crack sprouting and extension. Fig. 12a – 12b and Fig. 12d – 12e show the SEM images of crack extension after indentation tests for $MoSi_2$ and $MoSi_2$@Nb materials, respectively. It can be seen that the crack extension mode of $MoSi_2$ material is mainly transgranular fracture, while the crack extension mode of $MoSi_2$@Nb material is mainly intercrystal fracture. A more tortuous crack extension path is observed from Fig. 12e with intergranular fracture, crack deflection and crack bridging. Compared with the $MoSi_2$ material, the cracks of $MoSi_2$@Nb material absorb more energy during the extension, so it exhibits higher fracture toughness. Fig. 12c shows the fracture morphology of $MoSi_2$ material. After holding at 1450 °C for 10 min, the grain of pure $MoSi_2$ is relatively coarse, and some holes are distributed at the interface. The fracture surface is relatively flat, with obvious features of deconvolution fracture and crystal penetration fracture. Fig. 12f shows

Table 2 Fracture toughness K_{IC} of $MoSi_2$ and $MoSi_2$@Nb prepared by different methods (MPa·m$^{1/2}$)

Twice-coated $MoSi_2$@Nb	Once-coated $MoSi_2$@Nb	Mixed $MoSi_2$
5.75	4.77	3.32

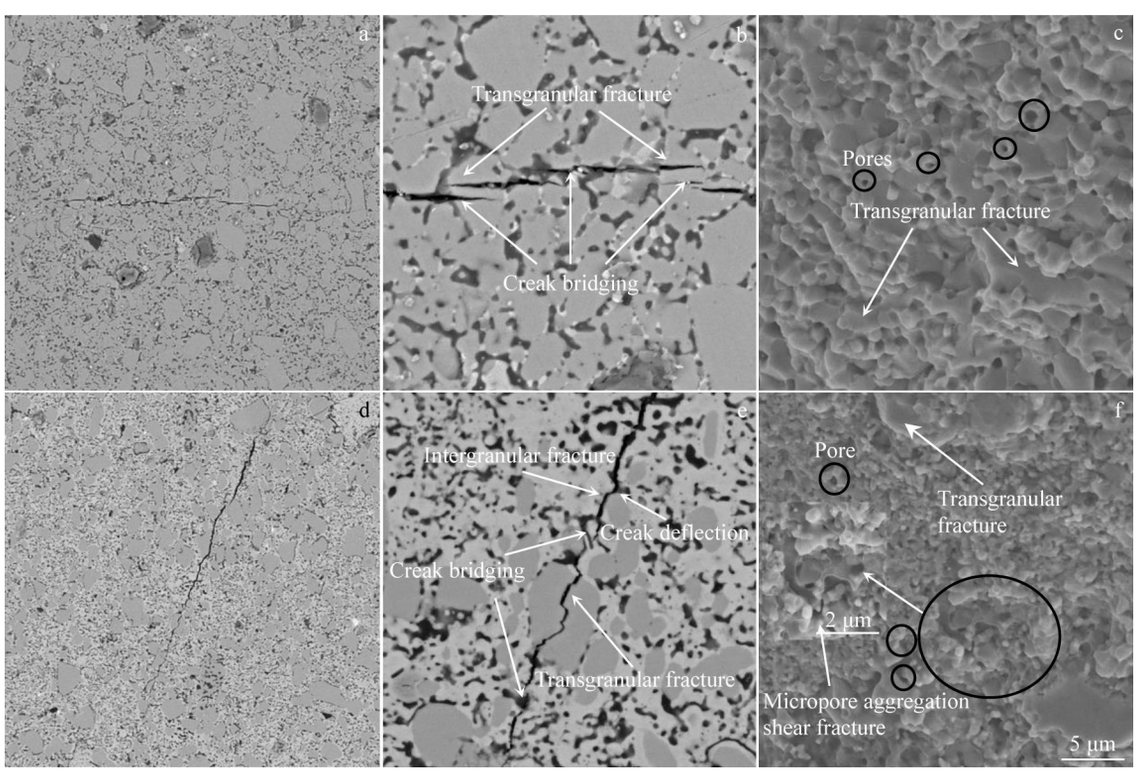

Fig.12 SEM images of crack and fracture morphologies of $MoSi_2$ (a–c) and $MoSi_2$@Nb (d–f) materials

the fracture morphology of $MoSi_2$@Nb material, and the grain size of $MoSi_2$ is obviously reduced compared with that in Fig. 12c. Besides, with the coating of Nb silicide, the fracture morphology of $MoSi_2$@Nb material is mainly crystalline intergranular fracture. There is also a small amount of micropore aggregation shear fracture, the generation process of which is that the dislocation slides to the front of the brittle second phase to generate dislocation plug group, and finally micropores are generated. The dimple fracture is formed through nucleation and aggregation of micropores. As previously stated, reaction products $(Mo, Nb)_5Si_3$ and $NbSi_2$ phases are uniformly wrapped around the $MoSi_2$ grains. In this way, the effect of Nb, Nb_5Si_3, Mo_5Si_3 and $NbSi_2$ multiphase toughening $MoSi_2$ is formed, and the great toughness of Nb phase can make the crack tip form a plastic deformation zone or a ductile crack bridging. However, different fracture forms between the phases with slightly better toughness. $MoSi_2$ and $(Mo, Nb)_5Si_3$ can produce synergistic effects and play a role in diffusion strengthening at the grain boundaries of $MoSi_2$. The crack tip is deflected as it expands into hard and brittle phases, resulting in a toughening effect.

3 Conclusions

1) When the concentration of SDS is 2 mmol/L, the concentration of CTAB is 3 mmol/L, and the pH value of Nb suspension is adjusted to 5, the twice-coated core-shell $MoSi_2$@Nb powder with relatively complete coating can be obtained by the electrostatic adsorption principle. The positive charge value of Nb suspension reaches the maximum Zeta potential value of 40.06 mV when the pH value is 5, which matches the Zeta potential value of −46.28 mV of the $MoSi_2$ suspension.

2) To remove the excess surfactant, the core-shell powder is calcined at 200 °C for 2 h under Ar atmosphere. $NbSi_2$ phase forms at the interface between $MoSi_2$ and Nb after calcination at 200 °C for 2 h, indicating that Nb has strong activity and reacts with Si. When twice-coated $MoSi_2$@Nb powder is sintered into solid materials by SPS at 1450 °C for 10 min under uniaxial pressure 40 MPa, Nb, Mo and Si ternary diffusion system is very active. Therefore, Nb and $MoSi_2$ react sharply to form Nb_5Si_3, $NbSi_2$ and Nb_3Si phases, but there are still Nb phase in the XRD pattern of $MoSi_2$@Nb material. The core-shell structure is preserved after sintering. Subsequent work should focus on reducing the degree of Nb reaction.

3) After SPS at 1450 °C for 10 min under uniaxial pressure of 40 MPa, fracture toughness increases from 3.32 $MPa \cdot m^{1/2}$ of $MoSi_2$ material to 5.75 $MPa \cdot m^{1/2}$ of $MoSi_2$@Nb material. Besides, the failure mode is brittle fracture.

References

1 Liang H, Peng F, Chen H *et al. Materials Science and Engineering A*[J], 2018, 711: 389

2 Sharif A A. *Journal of Materials Science*[J], 2010, 45(4): 865

3 Wang Dezhi, Liu Xinyu, Zuo Tieyong. *Rare Metal Materials and Engineering*[J], 2002, 32(1): 48 (in Chinese)

4 Zhu L, Chen P, Cai Z M *et al. Transactions of Nonferrous Metals Society of China*[J], 2022, 32(3): 935

5 Thakur A, Gangopadhyay S. *International Journal of Machine Tools and Manufacture*[J], 2016, 100: 25

6 Chou T C, Nieh T G. *Journal of Materials Research*[J], 1993, 8(1): 214

7 Yuan Xiaohong, Wei Yan, Han Yong *et al*. *Journal of Alloys and Compounds*[J], 2023, 968: 172178

8 Nie X W, Lu Q. *Ceramics International*[J], 2021, 47(14): 19700

9 Esmaeily S, Kermani M, Razavi M *et al. International Journal of Refractory Metals and Hard Materials*[J], 2015, 48: 263

10 Todai M, Hagihara K, Kishida K *et al. Scripta Materialia*[J], 2016, 113: 236

11 Pill L S, Pan J, Sasaki G *et al. Composite Interfaces*[J], 2012, 5(5): 405

12 Dasgupta T, Umarji A M. *Intermetallics*[J], 2008, 16(6): 739

13 Zenk C, Gibson J S K L, Maier-Kiener V *et al. Acta Materialia*[J], 2019, 181: 385

14 Xiao L, Kim Y S, Abbaschian R *et al. Materials Science and Engineering A*[J], 1991, 144(1–2): 277

15 Zhang N, Li Q, Yang K *et al. Ceramics International*[J], 2020, 46(11): 18832

16 El-Toni A M, Habila M A, Labis J P *et al. Nanoscale*[J], 2016, 8(5): 2510

17 Zhu Y, Zhu R, Xie J *et al. Journal of Solid State Chemistry*[J], 2019, 277: 519

18 Niihara K, Morena R, Hasselman D P H. *Journal of Materials Science Letters*[J], 1982, 1: 13

19 Anstis G R, Chantikul P, Lawn B R *et al. Journal of the American Ceramic Society*[J], 1981, 64: 533

20 Santos C D, Coutinho I F, Amarante J E V *et al. J Mech Behav Biomed Mater*[J], 2021, 116: 104372

21 Makavipour F, Pashley R M. *Chemical Engineering Journal*[J], 2015, 262: 119

22 Müller B R. *Carbon*[J], 2010, 48(12): 3607

23 Kosmulski M, Mączka E. *Journal of Molecular Liquids*[J], 2022, 355: 118972

24 Sizochenko N S, Mikolajczyk A, Syzochenko M *et al. NanoImpact*[J], 2021, 22: 100317

25 Kuchino J K, Kurokawa K, Shibayama T *et al. Vacuum*[J], 2004, 73(3–4): 623

26 Yao D, Yang J, Gong W *et al. Materials Science and Engineering A*[J], 2010, 527(26): 6787

27 Xiao L, Abbaschian R. *Materials Science and Engineering A*[J] 1992, 155: 135

28 Rao K T V, Ritchie R O, Soboyejo W O Metall. *International Journal of Fatigue*[J], 1993, 15(4): 342

SPS烧结制备$MoSi_2$@Nb核壳结构材料及其表征

罗佳军[1]，全慈旺[1]，张建军[1,2]，陈水香[1]，张茜彤[1]，韩孟瑶[1]，梁炳亮[1]，陈卫华[1]

(1. 南昌航空大学 材料科学与工程学院，江西 南昌 330063)

(2. 南昌航空大学 江西省航空材料表面技术工程研究中心，江西 南昌 330063)

摘　要：采用静电层自组装法制备了核壳$MoSi_2$@Nb粉体。采用表面活性剂SDS（$CHSO_4Na$）和CTAB（$C_{19}H_{42}BrN$）对2种颗粒表面进行改性，使其带电，并用Zeta电位计测试悬浮液的Zeta电位。采用扫描电镜、透射电镜和能谱仪对合成材料的物相、形貌、结构和元素分布进行了表征。结果表明：当SDS浓度为2 mmol/L，CTAB浓度为3 mmol/L，Nb悬浮液pH值为5时，二次包覆后涂层效果较好。在200 ℃氩气中煅烧2 h后，Nb与$MoSi_2$的界面处发现了$NbSi_2$相，表明Nb具有高活性并与Si反应。在1450 ℃单轴压力40 MPa下放电等离子烧结2 h后，$MoSi_2$@Nb材料中仍保留了核壳结构。然而，Nb与$MoSi_2$反应强烈，大部分Nb相发生反应，这个问题在后续研究中亟待解决。与$MoSi_2$材料的断裂韧性（K_{IC}=3.32 MPa·$m^{0.5}$）相比，$MoSi_2$@Nb材料的K_{IC}显著提高至5.75 MPa·$m^{0.5}$。

关键词：核壳结构；静电层自组装；放电等离子烧结；断裂韧性

作者简介：罗佳军，男，1997年生，硕士，南昌航空大学材料科学与工程学院，江西 南昌 330063，E-mail：2318460724@qq.com